JOURNAL OF GEOPHYSICAL RESEARCH, VOL. 105, NO. D13, PAGES 17,417–17,436, AUG, 2000

On the hydrological cycle under paleoclimatic conditions as derived from AGCM simulations

Gerrit Lohmann

Max-Planck-Institute for Meteorology, Hamburg, Germany

Stephan Lorenz

Department of Geoscience, University of Bremen, Germany

Abstract. The atmospheric hydrological cycle is compared for different time slices of the late Quaternary. Simulations have been conducted with an atmospheric circulation model at T42 resolution, and we have performed a global evaluation of the atmospheric water vapor transport. The water export from the Atlantic catchment area, important for driving the large-scale thermohaline ocean circulation, is analyzed in detail. For the Last Glacial Maximum (LGM), we examine the model's sensitivity with respect to tropical cooling relative to the CLIMAP reconstruction which is motivated by recent data. We find that the LGM experiment with tropical cooling is in better agreement with proxy data available. Our experiments indicate that the water vapor transport is strongly affected by three mechanisms: continental drying, eddy moisture transport, and changes in the tropical circulation. Except for the continental drying and the blocking effect of the Laurentide ice sheet, the hydrological cycle is substancially different for both LGM experiments. We find that the hydrological system is rather sensitive to tropical temperature change which is important to understand paleoclimate and future climate changes.

1. Introduction

The hydrological cycle describes the transport of water in all three phases on the global scale. Summing up all water volume contributions, about 14×10^{17} m^3 water are on the Earth and are stored in different components of the climate system. Most of the water (more than 97%) is in the salty oceans, and about 2% is stored in the glaciers. The remainder is unevenly divided between the reservoirs of groundwater, lakes and rivers, the atmosphere, and soil [*Baumgartner and Reichel,* 1975; *Peixoto and Oort,* 1992]. The atmosphere is a central subsystem in the global climate system, because it has the highest mobility and it connects the other subsystems.

Dansgaard et al. [1993] used stable isotope measurements from the full length of the 250 kyr (thousands of years) Greenland ice core record (Greenland Ice Sheet Project) to examine climate stability during glacial periods. They found that apart from the most recent 10,000 years, instability dominated the North Atlantic climate over the last 230 kyr. Other paleoclimate proxies point out an extreme rapidity in the changes of aridity, dust, and chemical composition, as recorded by Greenland ice cores [*Mayewski et al.,* 1993], or by marine sediment cores [*Lehman and Keigwin,* 1992], implying that events at the end of the last glaciation could have been responses to a threshold in the North Atlantic climate system.

One possible mechanism for such a threshold is associated with the hydrological cycle [*Birchfield,* 1989; *Broecker et al.,* 1990; *Zaucker et al.,* 1994; *Rahmstorf,* 1995]. Besides the exchange of energy and momentum between atmosphere and ocean, the freshwater flux is one of the main driving forces for the oceanic thermohaline circulation (THC). While air-sea heat fluxes damp sea surface temperature anomalies quite effectively, there is no direct feedback in the atmosphere for removing sea surface salinity anomalies, because precipitation and evaporation are not dependent on ocean salinity. Numerical experiments suggest that the THC is very sensitive to the atmospheric freshwater forcing [*Manabe and Stouffer,* 1995; *Rahmstorf,* 1996; *Weaver et al.,* 1998]. Sensitivity experiments with a highly idealized model of the THC suggest that this sensitivity is even stronger during glacial times due to the temperature dependence of the thermal expansion coefficient [*Prange et al.,* 1997].

Warren [1983] suggested that the low surface salinities in the Pacific are due to an excess of precipitation over evaporation and that this can be the reason for the absence of deep water formation there. Because the salinity characteristic is affected by the interbasin transport of water vapor it is therefore conceivable that the hydrological cycle is responsible for the difference between the thermohaline circulation in the North Atlantic and Pacific Oceans. It has been argued [*Birchfield,* 1989; *Broecker et al.,* 1990; *Zaucker et al.,* 1994] that the interbasin water vapor transport provides for multiple equilibria of the climate system. A recent sensitivity study [*Weaver et al.,* 1998] confirms this idea: By changing the Atlantic catchment of a few rivers, the *Weaver et al.* [1998] model is able to enhance or to slow down the Atlantic thermohaline circulation.

The hydrological cycle and its associated distribution of moisture is furthermore of interest because of its important influence on the terrestrial climate, distribution of vegetation and deserts, and the growth of ice sheets. These geographical features are documented by the proxy data available, as for example lake levels and vegetation types [*Crowley and North,* 1991; *Farrera et al.,* 1999]. Further links of the water vapor transport with climate are due to the ice sheets and the water's isotopic compositions [*Werner et al.,* 2000].

Atmospheric general circulation models (AGCMs) simulate the global hydrological cycle for the present climate and are therefore appropriate tools for analyzing changes in moisture and water vapor transport. The aim of this paper is to examine the water transport and associated freshwater flux for different paleoclimatic conditions simulated by an atmospheric circulation model. *Zaucker and Broecker* [1992] have proposed a method to obtain present-day water transport. This method is applied here to the paleoclimatic simulations. To examine the response of the hydrological cycle to changed boundary conditions, we apply several sensitivity experiments with our AGCM. The simulation of paleoclimates provides a possibility elaborating the AGCM response to changed boundary conditions. We analyze here the water vapor paths showing the net evaporative and net precipitative regions on earth for different time slices of the late Quaternary. The late Quaternary is the time span of the last 800 kyr where the 100 kyr cycle is found to be dominant for the glacial-interglacial changes [*Hays et al.,* 1976].

Our experiments performed have been designed to capture important features of climate stages during the last 100 kyr cycle [*Imbrie et al.,* 1984]: The Glacial Inception at 115 kyr before present (B.P.) marks the begining of the last glacial, the Last Glacial Maximum (21 kyr B.P.), the cold extreme of the last glacial, and the Climate Optimum (6 kyr B.P.) represents the warm interglacial. The simulations provide snapshot views of the climate states forced by sea surface temperatures, orography, and other conditions, such as CO_2, which are obtained from proxy data.

Because of its controversial debate, we focus especially on the role of the tropical cooling during the Last Glacial Maximum (LGM). There is a growing body of evidence that the LGM temperature reconstruction as proposed by the Climate/Long-Range Investigation, Mapping, and Prediction (CLIMAP) project [*CLIMAP,* 1976, 1981] must be revised over large areas of the globe. Since the reconstructed temperatures from a diverse set of archives (corals, tropical ice cores, noble gas from groundwater, marine sediment pore fluids, snowline depression, pollen studies) indicate a cooling in the tropics relative to CLIMAP, we examine the role of tropical cooling in sea surface temperature for the hydrological system. The simulations performed can therefore be used to evaluate consistencies with terrestrial proxies available.

The paper is organized as follows: In section 2. the methodology is described. The hydrological cycle of our experiments are shown in section 3.. The results are discussed in section 4. where we have focused on our Last Glacial Maximum experiments performed. Finally, the conclusions are given in section 5..

2. Model Description and Methodology

The atmospheric circulation model ECHAM 3 is briefly introduced in section 2.1.. For our paleoclimatic simulations, insolation and CO_2 forcing (section 2.2.), and the lower boundary conditions (section 2.3.) are described in detail. The method of water vapor transport is examined in section 2.4..

2.1. General Circulation Model ECHAM 3

The ECHAM model is an atmospheric general circulation model initially developed at the European Centre for Medium-Range Weather Forecasts (ECMWF) and later modified for climate application [*Roeckner et al.,* 1992]. The model is based on the primitive equations and includes radiation, a hydrological cycle (with clouds), and a soil model. The formation of clouds and precipitation are beyond the scale of the model resolution and are therefore parameterized. The ECHAM 3 model considers cloud water formation and transport, partitioning of liquid/ice phase with sedimentation of ice crystals, and evaporation of cloud water and raindrops.

The model equations are solved in the spectral domain with triangular truncation at the wavenumber 42. The physical parameterizations are calculated on the corresponding Gaussian grid of 128×64 grid points shown as rectangles in Plate 1. The vertical representation is realized by 19 hybrid levels, where the two lowest layers are terrain-following layers and the top two layers are at isobaric surfaces up to 10 hPa.

2.2. Insolation and CO_2 Forcing

Our simulations use prescribed sea surface temperature, orography and ice sheet distribution, insolation, and CO_2 concentration. At the top of the atmosphere

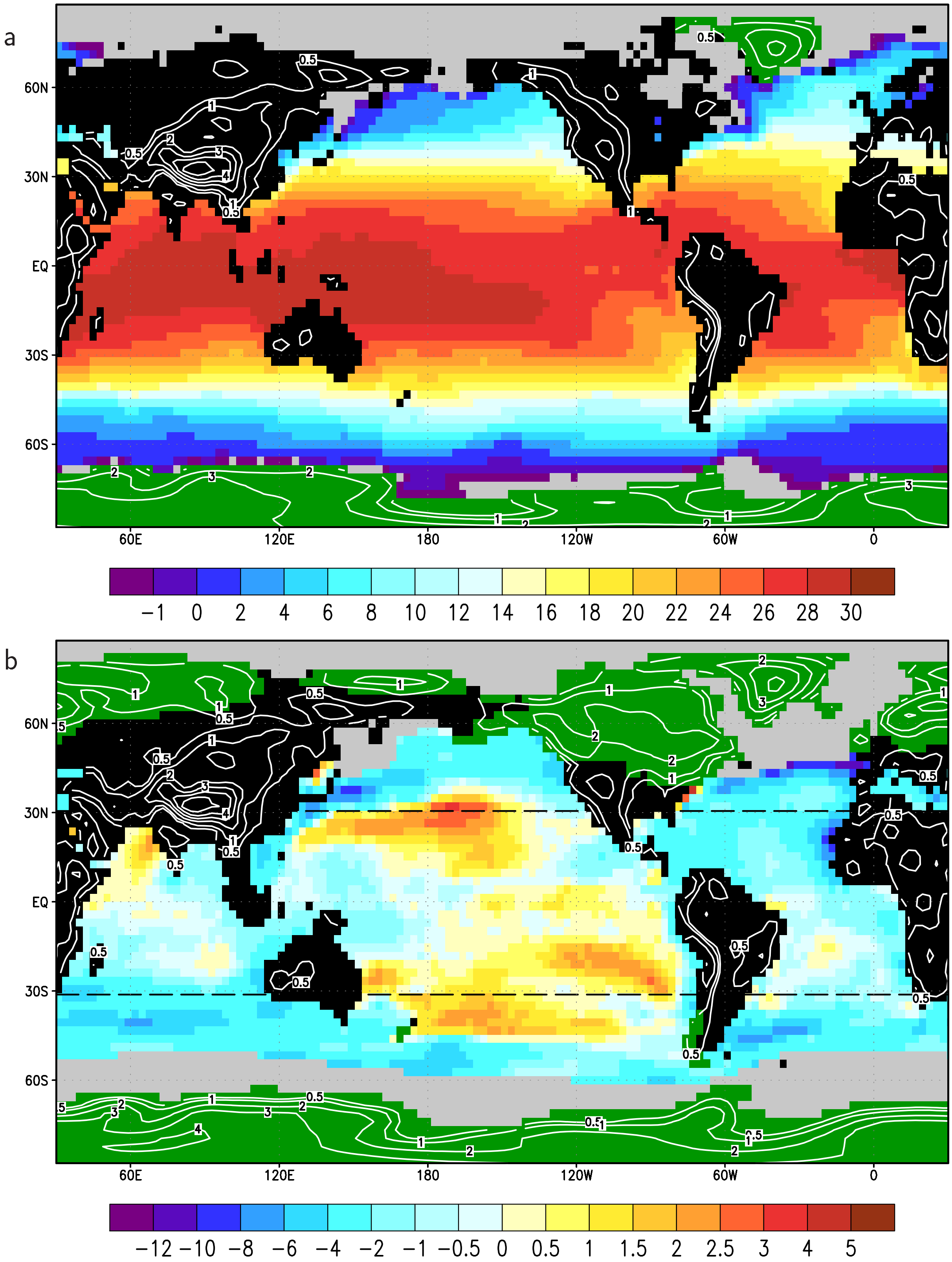

Plate 1. Boundary conditions (February) for the control (0 kyr B.P., Plate 1a) and LGM (21 kyr B.P., Plate 1b) runs. The continents are shown with contour lines marking the smoothed terrain heights (10^3m) in the model. Plate 1a shows the sea surface temperature for the control run, sea ice cover (grey), land ice cover (green), and topography (black). Plate 1b shows the SST anomalies for the LGM as supplied by *CLIMAP* [1981]. In the LGM.N run, the sea surface temperature anomaly in Plate 1b has been modified between 30°N and 30°S indicated by the dashed lines (see text and Table 1 for the details).

Table 1. List of Experiments Performed and Main Results

	Control	GI	CO	LGM.O	LGM.N
Time Slice (year)	0 B.P.	115,000 B.P.	6,000 B.P.	21,000 B.P.	21,000 B.P.
			Input Parameter of the Simulations[a]		
Eccentricity (%)	1.67	4.14	1.87	1.90	1.90
Obliquity (°)	23.45	22.41	24.11	22.95	22.95
Date of perihelion	Jan. 3	Jan. 14	Sept. 20	Jan. 15	Jan. 15
CO_2 (ppm)	345	345	280	200	200
Orography	Plate 1a	Plate 1a	Plate 1a	Plate 1b	Plate 1b
Sea level	present	present	present	–120 m	–120 m
SST/Sea ice	present	present	present	CLIMAP	CLIMAP, trop. cooling
			Water vapor transport out of the Atlantic catchment[b]		
North America					
→ Arctic	–0.117	–0.106	(–0.115)	–0.080	–0.069
30° – 50°N	–0.155	(–0.152)	(–0.144)	–0.182	–0.128
0° – 30°N	0.252	(0.257)	0.235	0.296	0.209
South America	0.096	0.077	0.117	0.145	0.112
Southern Ocean 30°S	0.305	0.273	0.283	0.316	0.232
North Africa	–0.136	–0.124	(–0.135)	–0.153	–0.122
South Africa	–0.168	–0.134	–0.138	–0.108	–0.081
Asia	0.100	(0.097)	0.109	0.081	0.057
Net tropical Atlantic	0.554	0.527	0.575	0.828	0.589
Net northern Atlantic	–0.377	–0.339	–0.362	–0.513	–0.379
Net Atlantic	0.177	0.188	0.213	0.315	0.210

[a]Input parameter and boundary conditions used for the control integration (present climate), Glacial Inception (GI), Climate Optimum (CO), and Last Glacial Maximum (LGM.O and LGM.N).
[b]The water vapor transport (Sv $=10^9$ kg s^{-1}) over the drainage divides and 30°S. For the definition of the Atlantic catchment area, see the thick black line in Plate 2. The tropical and northern Atlantic water balances are defined by the sections at 30°N and 30°S in the Atlantic Ocean. Positive values indicate a net transport out of the Atlantic area. Parentheses are used for the values that are not significantly different from the present climate on a 95% level (t-test).

the insolation pattern was prescribed, following the astronomical theory of *Milanković* [1941]. The distribution of solar radiation depends on the Earth's orbit. The elliptical orbit of the Earth's motion around the Sun is characterized by three parameters: eccentricity, obliquity, and the date of the passage through the perihelion. These orbital parameters (Table 1, top) were taken from *Berger* [1978] to calculate the insolation patterns for the model runs.

The obliquity is the angle between the Earth's rotation axis and the normal to the ecliptic (the plane of the Earth's orbit), varying with a dominant period of about 40 kyr. The precession cycle with a main period near 20 kyr affects the date of the perihelion, when the Earth is next to the Sun and receives maximum insolation. The third parameter, the eccentricity of the Earth's orbit, has a main period of about 100 kyr. Although the eccentricity has a negligible influence on the annual mean insolation on the Earth, it strongly modulates the strength of the precession cycle.

The solar radiation at the time of the Climate Optimum (CO, 6 kyr B.P.) was enhanced over the Northern Hemisphere during JJA (June, July, August) of more than 20 Wm^{-2} compared to the modern distribution. This is mainly due to an increase in obliquity (24.1° in CO rather than 23.4° today). The increased tilt leads to a stronger seasonal cycle, i.e., more insolation in the summer and less in the winter season of the respective hemisphere. In the tropics the insolation anomalies are strongly tied to the precession cycle. During the CO, when the passage through the perihelion is September 20 rather than January 3 today, the precession accounts for a reduced tropical insolation during DJF (December, January, February) of about –20 Wm^{-2}.

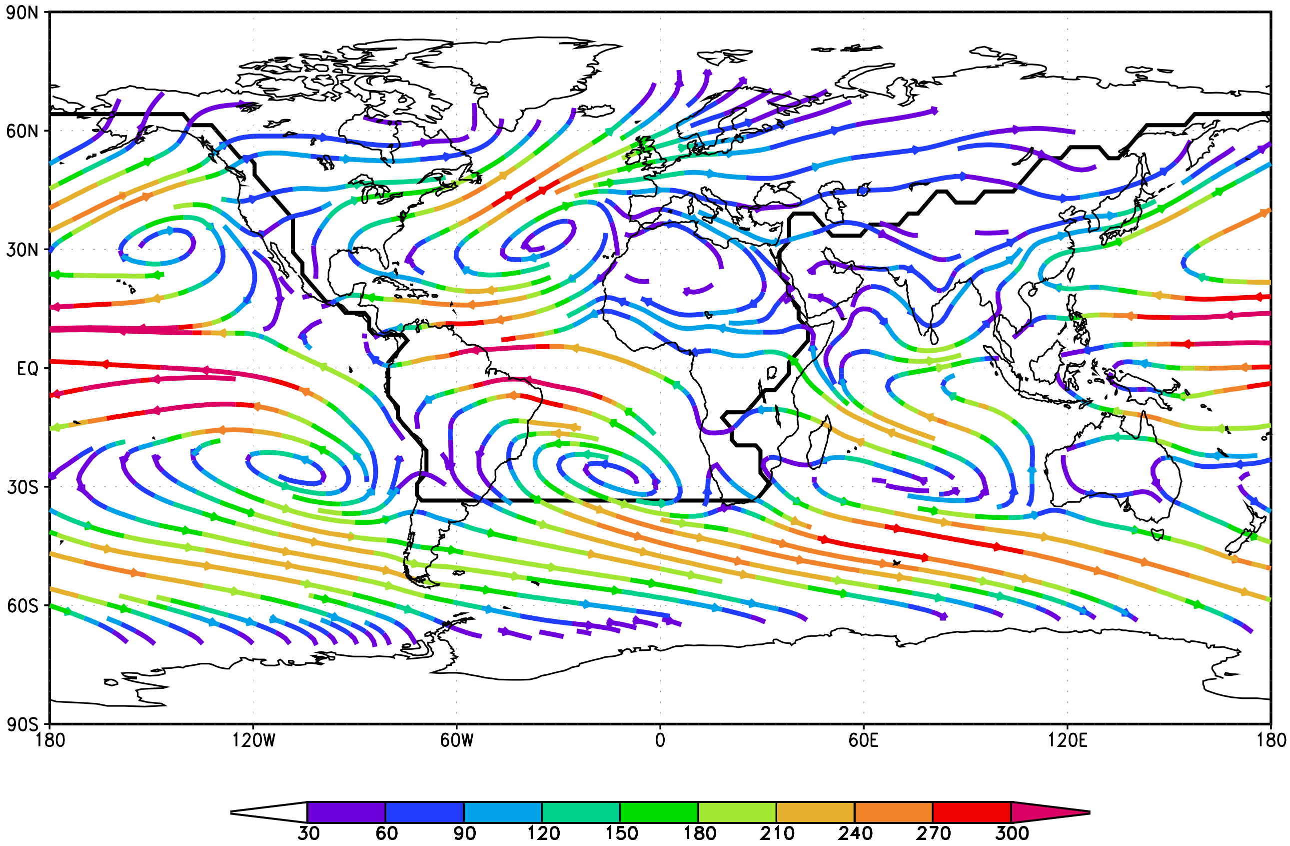

Plate 2. Streamlines of the vertically integrated water vapor transport for the simulation of the present climate (control run). The thick black line shows the Atlantic drainage divides. Sources and sinks of water vapor streamlines indicate net evaporative and net precipitative regions, respectively. Units are $\mathrm{kg\,m^{-1}\,s^{-1}}$ where values below 30 $\mathrm{kg\,m^{-1}\,s^{-1}}$ are suppressed.

The Glacial Inception (GI, 115 kyr B.P.) solar forcing exhibits almost the opposite pattern to the CO: a reduced Northern Hemisphere summer insolation is mainly due to a decreased obliquity (22.4°), whereas the increased tropical solar radiation during DJF is caused by the precession cycle. There is almost no change in insolation for the Last Glacial Maximum (LGM, 21 kyr B.P.) except for an insolation reduction of about 10 $\mathrm{Wm^{-2}}$ poleward of 60° during the respective summer season caused by reduced obliquity. The CO_2 concentration used for the CO and the LGM runs (Table 1, top) were chosen according to measurements from the Vostok ice core [*Barnola et al.,* 1987]. For the GI run, a modern value was used instead of 240 ppm.

2.3. Lower Boundary Conditions

The boundary conditions at the bottom of the atmosphere are given by the Earth's orography, the distribution of land, sea, sea ice, and ice sheets, vegetation, albedo, and sea surface temperature. The quantities, which are used for the different model runs are listed in Table 1 (top). Except for the runs LGM.N and GI, these boundary conditions were defined within the Paleoclimate Modeling Intercomparison Project PMIP [*Joussaume and Taylor,* 1995].

For the control run, the February surface boundary conditions are shown in Plate 1a, indicating sea surface temperatures (colors), the respective sea ice distribution (grey), ice sheets (green), and continents (black). The present climate sea surface temperatures are based on the AMIP [*Gates,* 1992] data set (Plate 1a). One should have in mind that present climate surface boundary conditions are not in radiative equilibrium with the high industrial level of CO_2. The GI and CO experiments use present-day surface boundary conditions as in the control run (Plate 1a) because global maps of the required paleoclimate boundary conditions are not available. One can further argue that the climate at these time slices is probably not too far away from an interglacial climate, as the modern climate state, and therefore the lower boundary conditions for our model may be close to the modern ones.

For the LGM, a global reconstruction of the surface conditions was supplied by *CLIMAP* [1976, 1981]. This reconstruction provides a first step for the analysis of the Last Glacial Maximum, since there is no other comprehensive data set available. The area covered by the glacial ice sheets is indicated by the green area in Plate 1b, where the thickness of the ice sheets is altered according to *Peltier* [1994]. The land-sea distribution is changed according to a sea level drop of 120 m. CLIMAP provides, furthermore, the sea ice distribution and sea surface temperature (SST) for February and August. The annual cycle of SST is approximated by a sinusoidal function, taking the values for February and August as extremes. Plate 1b shows the glacial SST anomaly for February as supplied by CLIMAP, indicating large regional differences in SST.

The tropical SSTs of the CLIMAP reconstruction are a subject of controversial debate. Geochemical studies provide some support for the hypothesis that the glacial SSTs in low latitudes were 2–4 K colder compared to CLIMAP [*Guilderson et al.,* 1994; *Schrag et al.,* 1996; *Pisias and Mix,* 1997]. Recent alkenone data indicate that the temperatures in the equatorial oceans dropped 4 K in the Atlantic, 2 K in the Indian, and relatively minor in the Pacific oceans during the LGM [*Bard et al.,* 1997].

Because of the large uncertainties in tropical SSTs during glacial times, we performed two experiments LGM.O and LGM.N with different SSTs prescribed. The experiment LGM.O uses the CLIMAP SST-forcing as in the work of *Lorenz et al.* [1996]. (In the LGM simulation of *Lorenz et al.* [1996] an error in the annual cycle of the SST field has been detected. Therefore the simulation has been repeated with the corrected forcing and only the revised simulation is analyzed here. Despite some incorrect spring and autumn SSTs the overall results for the JJA, DJF, and annually averaged quantities in the work of *Lorenz et al.* [1996] remain valid.) We performed a new LGM experiment (LGM.N) with an additional cooling in the tropics (30°S – 30°N) relative to the CLIMAP reconstruction which is motivated by recent data. The dashed lines in Plate 1a indicate the area of tropical cooling of 3 K compared to CLIMAP. In order to get a smooth transition, the neighboring latitudinal grid lines at 32° and 35° are cooled by –2 and –1 K relative to the CLIMAP values, respectively. Furthermore, we allow no positive SST anomalies in LGM.N. These anomalies are present in the CLIMAP reconstruction of the Pacific, Indian and Atlantic Oceans (Plate 1b) and can be caused by cartographic extrapolation from a few data points with high uncertainty [*Broccoli and Marciniak,* 1996]. The warming during LGM is also in conflict with alkenone thermometry [e.g., *Bard et al.,* 1997] and modeling studies [e.g., *Ganopolski et al.,* 1998]. The SST forcing in LGM.N, however, relies on the geographical pattern of CLIMAP. This is motivated by temperature reconstruction patterns on adjacent land areas (for a recent review, see *Farrera et al.* [1999]) showing the existence of CLIMAP-like patterns with moderate cooling on the Pacific and Indian Ocean regions.

2.4. Water Vapor Transport

In our paper we want to concentrate on the atmospheric water transport, the interbasin water exchange, and associated freshwater fluxes for the different time slices. Following *Zaucker and Broecker* [1992] the drainage divides for the Atlantic and Pacific/Indian Oceans are given by the direction of river flow where the freshwater flux over land leads to runoff into the oceans. The thick line in Plate 2 indicates the water divides over America, Asia, Africa, and the Southern Ocean which separates the area of the Atlantic Ocean from the other basins. The drainage divides are calculated from present-day orography.

The transport of water in the vapor phase is much larger than the transport of water by clouds in the condensed and solid phases which is almost irrelevant for the transport on the large scale. The vertically integrated transport of water vapor is connected with the surface freshwater flux in the stationary case [*Peixoto and Oort,* 1992; *Zaucker and Broecker,* 1992; *Wijffels et al.,* 1992] via its divergence:

$$\nabla \cdot \int_0^{p_s} \vec{v}\, q \, \frac{dp}{g} \quad = \quad E - P \quad . \tag{1}$$

∇ denotes the two-dimensional divergence operator, $\vec{v}$ is horizontal velocity, q is the water vapor mixing ratio, p is pressure, and g is the acceleration due to gravity at the Earth's surface. The freshwater flux $E - P$ consists of evaporation E and precipitation P, p_s denotes the surface pressure.

For our analysis we separate the horizontal freshwater transport over the Atlantic drainage divides into sections (listed in Table 1): The easterly transport within the Hadley cells (0°–30°N, 0°–30°S) over America and Africa, the westerly transport in midlatitudes over North America where the water reaches the North Atlantic Ocean, the transport over North America between 50°N and Bering Strait corresponding to the Arctic Ocean catchment area, and the water transport over Asia. The Atlantic drainage divides are completed by the Southern Ocean and part of South America (Plate 2). Furthermore, we divide the Atlantic catchment area into the tropical Atlantic (30°S – 30°N) and the northern North Atlantic (north of 30°N) as listed in Table 1. To detect the significance for the change in water transport over these sections, we apply a statistical t-test to the last 10 yearly means of the respective model runs.

3. Results

3.1. Present-Day Hydrological Cycle

The water vapor transport is calculated for the different time slice experiments listed in Table 1. For the control integration (present climate), water vapor paths are shown in Plate 2. The streamlines in the figure give direction, and the color of the streamlines indicates the amplitude of net water vapor transport $\int \vec{v}\, q\, g^{-1} dp$. Along a hypothetical water vapor path, the change in color from red to blue (blue to red) indicates a loss (gain) of water resulting in net precipitation (evaporation). Furthermore, the lines diverge over net evaporative regions and converge over regions with net precipitation (equation (1)).

The water vapor transport reflects characteristics of the general circulation of the lower troposphere. In the tropics, strong easterlies are observed, especially over the Atlantic and Pacific Oceans. Furthermore, the subtropical highs over the Atlantic and Pacific are sources of water vapor, and this moisture is transported to the tropics and high latitudes. For today's climate we find (column 1 of Table 1) that atmospheric water vapor is transported out of the Atlantic basin over South/Central America, the Southern Ocean, and Asia, whereas water vapor is transported into the Atlantic basin over Africa and North America across the drainage divides. For our interpretation of the water vapor transport as an oceanic freshwater forcing, we have assumed a closed water balance: The net precipitation over the ice sheets leads on the long term to additional runoff into the ocean.

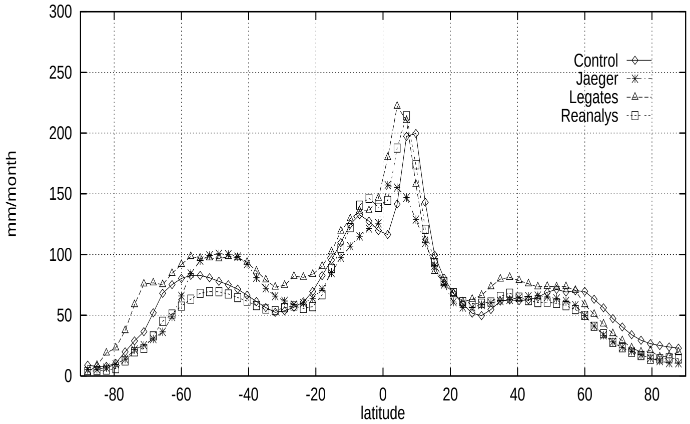

Figure 2: Zonal mean precipitation for the control integration, the climatological estimates of *Jaeger* [1976] and *Legates and Willmott* [1990], and ECMWF reanalysis data [*Gibson et al.,* 1997].

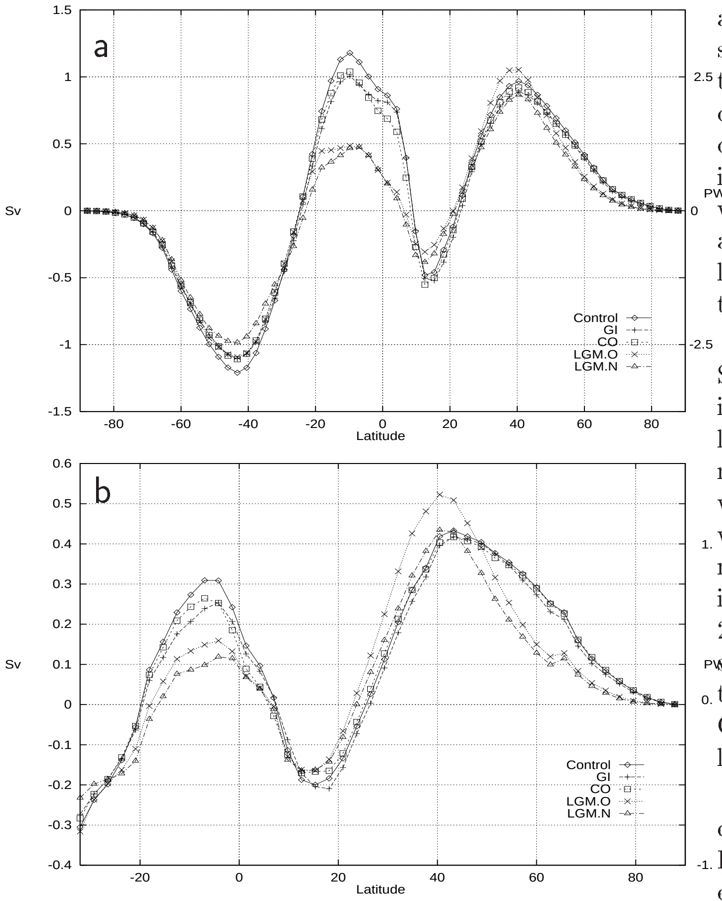

Figure 1: Meridional mass transport for the model experiments. (a) Global transport and (b) transport in the Atlantic catchment area. A mass transport of 1 Sv corresponds to a latent heat transport of 2.5 PW, indicated on the right-hand side of the panels.

Furthermore, we evaluate the zonal mean meridional latent heat transport according to equation (1). Evaporation of water from the ocean surface is a major heat loss for the ocean, while condensation of water vapor is a major heat source for the atmosphere. In the atmosphere the latent heat transport is linked to the mass transport: the water transport of 10^9 kg s^{-1} (= 1 Sv) corresponds to 2.5 PW (PW= 10^{15} W). For the present climate we find (Figure 1a) two maxima and two minima of the northward transport, which are associated with the equatorward transport by the Hadley cells and poleward transport by eddies in midlatitudes. This large-scale feature is also seen in precipitation rates of the model and observations (Figure 2).

Figure 1a shows a water vapor transport of about 0.8 Sv from the Southern to the Northern Hemisphere. This is a consequence of the unevenly distributed portion of land and sea over the hemispheres, which affects the northward shift of the Hadley cell. For the ocean freshwater forcing, it is useful to calculate the atmospheric water vapor mass transport within the Atlantic catchment area (Figure 1b), revealing a southward transport in the Northern Hemispheric Hadley cell and south of 20°S, and a northward transport in the Southern Hemispheric Hadley cell and north of about 25°N. Note that the southward export of water vapor into the Southern Ocean at 30°S in Figure 1b is identical with the values listed in Table 1.

The global distribution of precipitation minus evaporation (P–E) for the control simulation is shown in Figure 3. The subtropical highs in the Atlantic, eastern Pacific, and southern Indian oceans are connected to the downward branch of the Hadley circulation. In this area the lack of clouds leads to massive evaporation and Plate 2 indicates a source of strong water vapor divergence. Close to the equator, a band of high net precipitation is associated with the Intertropical Convergence Zone (ITCZ), which is centered north to the equator due to the unevenly distributed land areas. The ITCZ has a characteristic two-band structure in

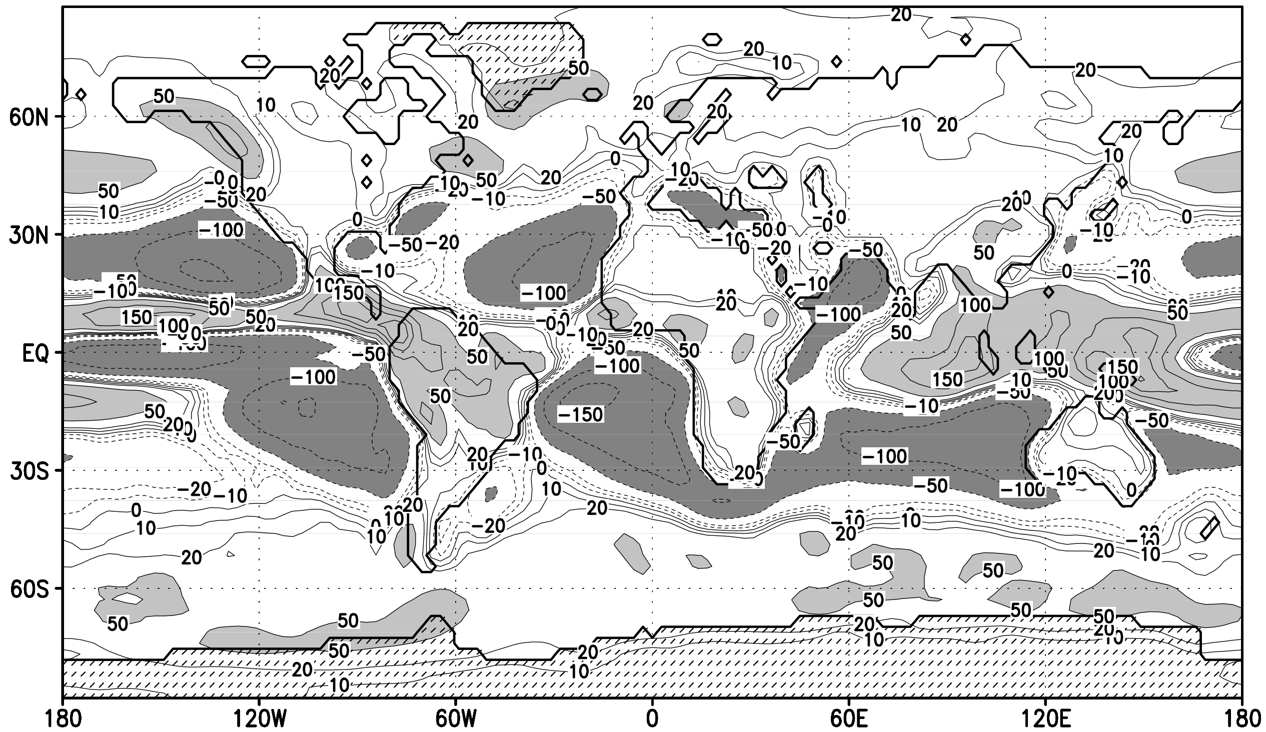

Figure 3: Precipitation minus evaporation for the control run. The contour lines are at (±) 0, 10, 20, 50, 100, and 150 mm/month, a 9-point filter has been used. Dashed lines are used for areas of net evaporation. Areas with values of more than 50 or less than –50 mm/month are lightly and darkly shaded, respectively.

the western Pacific and is relatively wide in the eastern Indian and southeast Asian regions. In the Indian Ocean and adjacent land areas, the net precipitation has a strong seasonal cycle by the monsoon circulation. The moisture originates from the tropical western Indian Ocean, where evaporation dominates over precipitation throughout the whole year (Figure 3). Poleward of 45°, precipitation is over evaporation with maximum amounts over mountain ranges.

3.2. Glacial Inception and Climate Optimum Experiments

The Glacial Inception (GI, 115 kyr B.P.) time slice with a reduced Northern Hemisphere summer insolation is associated with the onset of the last glaciation, whereas the Climate Optimum (CO, 6 kyr B.P.), with intensified northern hemisphere summer insolation, represents the warmest climate in the last glacial cycle [*Imbrie et al.,* 1984; *Berger,* 1978]. The CO stage lags some thousands of years behind the extreme insolation pattern [*Berger,* 1978], which is probably due to the time required for the ice sheets to melt.

The GI and CO experiments exhibit the model response to insolation changes. Along with a reduced JJA insolation in GI, surface temperature decrease by about 2° over wide areas of the Northern Hemisphere continents in summer and associated weakened monsoon circulation. The annual mean temperature tendency for GI is cooling except for the latitude band between 0° and 50°N. During the CO, JJA surface temperatures increase over the northern continents by about 2 K. Caused by insolation, the annual mean surface temperatures tend to increase between 40°−70°N and 10°−40°S and to decrease elsewhere. The different CO_2 concentrations in the CO and GI experiments (Table 1, top) make the summer warming in CO less than summer cooling in GI. The precipitation anomaly in CO has also the opposite sign to GI with an increased summer monsoon precipitation and less precipitation in the west and east of Southeast Asia [*Lorenz et al.,* 1996]. Correspondingly to the temperature change, the moisture over India and northeastern Africa has increased during the CO.

For the GI the drop of JJA temperature leads to a reduced high-pressure system over the North Pacific and a reduced import of water over the American continent (Table 1). The increased tropical insolation during winter makes the tropical land areas about 1 K warmer and enhances Southern Hemisphere precipitation relative to Northern Hemisphere precipitation on land.

For the CO the export over the Asian continent is enhanced (Table 1) due to warmer JJA temperatures. During DJF the land areas over Africa and Asia are much colder (–2K), and precipitation is enhanced over the Indian Ocean and reduced over South Africa and South America. The circulation over the African continent and the western Indian Ocean in the GI and CO experiments has shifted eastward such that the import of water vapor over the South African continent is decreased, compensating for a decreased export over the

Southern Ocean (Table 1).

We find, however, that the overall changes in the hydrological cycle for the GI and CO experiments are mainly caused by the change of the seasonal cycle. The annual averaged meridional water transport (Figure 1) during GI and CO differ only slightly from the present-day climate, which is also due to the unchanged (modern) SST chosen.

3.3. Last Glacial Maximum Experiments

In the late Quaternary the Last Glacial Maximum (21 calendar kyr B.P., approximately 18 ^{14}C kyr B.P.) is the most recent extremely cold climate, with a maximum extent of ice in the Northern Hemisphere, and is, furthermore, relatively well documented by proxies. Figure 4 shows the modeled anomalous near-surface air temperatures of the Last Glacial Maximum minus the control climate for LGM.O and LGM.N. Both experiments show a strong temperature reduction of more than 20 K in the area of the glacial ice sheets over northern Europe and America. The temperature drop is, on one hand, due to the change in albedo associated with the presence of ice and, on the other hand, due to the altered ice sheet topography with the 3000 m change in surface elevation leading to temperature differences in accordance with the lapse rate. Near the ice caps, the temperature drop is about 10 K (Figure 4). Between Greenland and Europe, where the CLIMAP reconstruction prescribes sea ice during the whole year, the isolation effect of sea ice from the warm ocean and winds coming from the glacial ice sheets cause a huge temperature drop of more than 30 K. The temperature changes over the ice-free regions of the ocean are mainly due to the the local SSTs and are more moderate.

The near-surface temperatures in Figures 4a and 4b differ strongly in the tropics where the SST-forcing has been changed. Over large continental areas, we find that the temperature drop between LGM.O and LGM.N is larger than the relative 3 K cooling over adjacent sea areas. In experiment LGM.N, the spatial distribution of the CLIMAP reconstructions remains visible due to the moderate cooling in the subtropical Pacific, Indian, and South Atlantic Oceans.

Figure 5 shows the zonal mean precipitation for control, LGM.O, and LGM.N simulations. The strongest reduction in precipitation during LGM is in the tropics and northern high latitudes. Convective precipitation, which is the main part of the tropical precipitation, decreases strongly for LGM.O and LGM.N (Figure 5). This feature can be understood by the reduced areas of deep convection which are related to the extent of the area with SST exceeding a critical threshold value [*Graham and Barnett,* 1987].

It is useful to analyze the vertically integrated water vapor $\int q\ g^{-1}\ dp$, which is also called precipitable water in the atmosphere [*Peixoto and Oort,* 1992]. The change in the vertically integrated water vapor (Figure 6) to first order follows the temperature change (Figure 4) due to the fact that colder air can hold less water vapor than warmer air. For LGM.O, the areas of decreased humidity include nearly all continental regions (with peak values over the ice caps and the southern American and southeastern Asian tropics), whereas enhanced humidity is located over the regions of low-latitude temperature increase. The CLIMAP reconstruction gives probably very warm SSTs in the subtropics, and correspondingly, the subtropical specific humidity (Figure 6) is more realistically simulated in LGM.N than in LGM.O. The differences in the two LGM experiments indicate that the reduction is much stronger in the warmer tropical temperatures, which is due to the nonlinear Clausius-Clapeyron equation.

Besides the temperature effect, the change in humidity is caused by anomalous atmospheric circulation. For the water vapor transport, three main effects can be identified.

3.3.1. Continental drying During the LGM the atmospheric freshwater transport north of 50°N toward the Arctic catchment area is effectively blocked off by the ice sheets and the Rocky Mountains (compare the orography in Plates 1a and 1b). The anomalous streamlines of vertically integrated water vapor transport (LGM.O – control) in Plate 3 indicate that a part of the water blocked by the ice sheets finds a path south of the Rocky Mountains toward the North Atlantic. The same is valid for the LGM.N run. Because of dryer conditions during the LGM over the Asian continent (Figure 4) the transport over Asia is slightly reduced (Table 1 and Plate 3).

During LGM, an anomalous cyclonic circulation centered over the northeast Atlantic and the Aleutian Islands, and anomalous anticyclonic circulation over central Asia and Canada is found (Plate 3). These streamlines of water vapor transport are strongly connected with stationary waves (not shown) induced by ice sheet orography. Additionally, the change in orography leads to a bifurcation of the jet stream from a relatively zonal (present climate) to a wave-like structure (LGM) following the altered vorticity balance.

3.3.2. Tropical transport In the tropics between 30°S and 30°N, the water vapor export is very sensitive to tropical SSTs. In LGM.O, more water vapor out of the tropical Atlantic area is exported relative to the control run (Table 1). This results from enhanced northward transport at 30°N (Figure 1b) and the transport over Central America (Plate 3). Plate 3 indicates that the export over Central America is connected to an anomalous circulation in the tropical East Pacific with a maximum at 100°W on the equator. Along with the anomalous transport, we find enhanced net evaporation in the Caribbean Sea and the region southwest of Central America (Figure 7a), and anomalous net precipitation for a region around the equator centered at 120°W. Corresponding patterns can be found for spe-

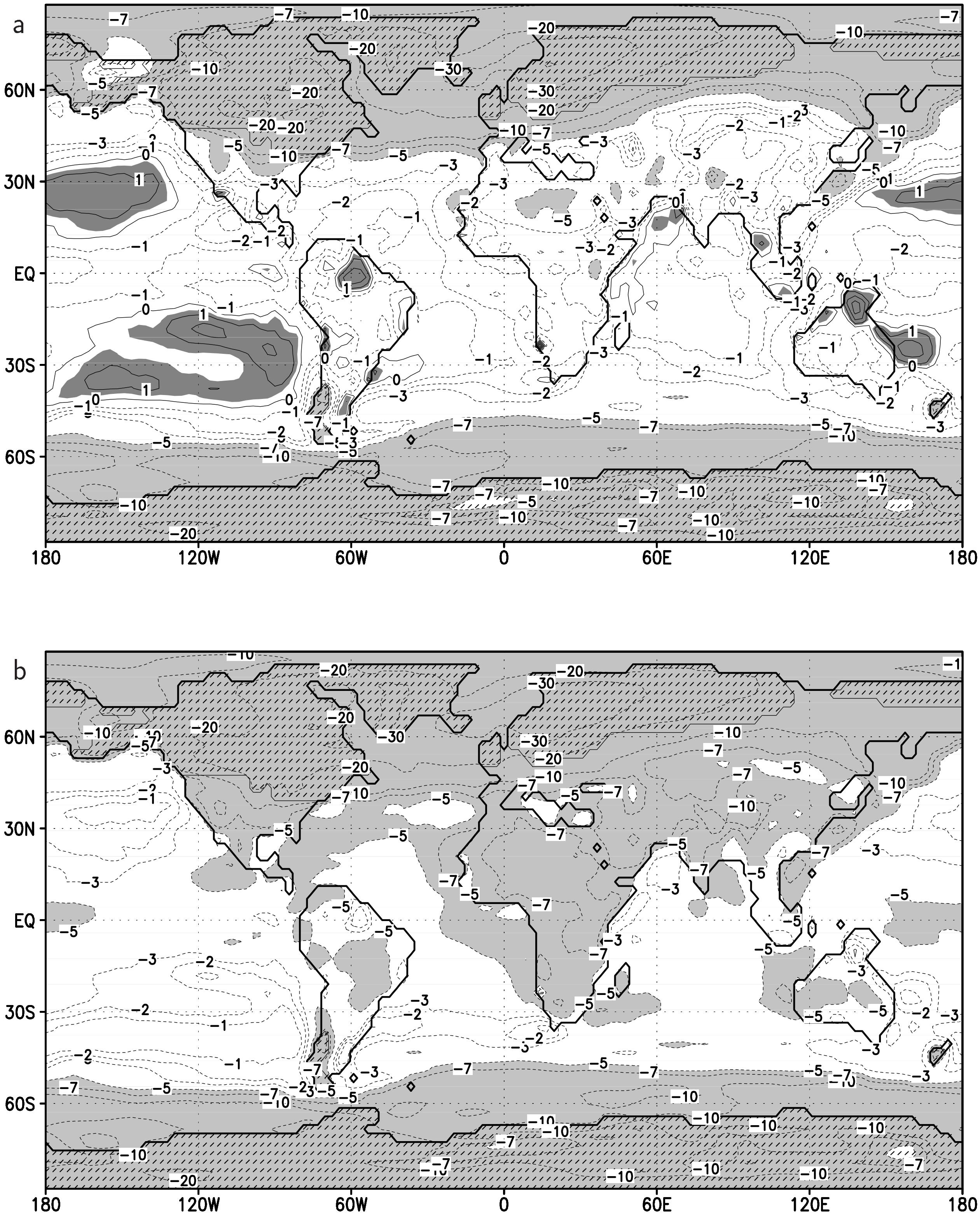

Figure 4: Anomalous glacial near-surface air temperature for the runs (a) LGM.O using the CLIMAP reconstruction and (b) LGM.N with tropical cooling relative to CLIMAP. The countour lines are shown at –30, –20, –10, –7, –5, –3, –1, 0, 1, 2, and 3 K. Areas of temperature change of more than +0.5 K are darkly, less than –5 K are lightly shaded, respectively.

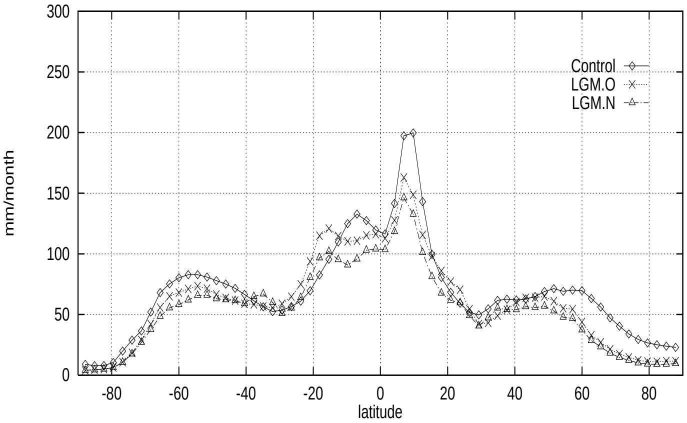

Figure 5: Zonal mean precipitation for control, LGM.O, and LGM.N simulations.

cific humidity (Figure 4a). A further analysis shows that the increased export of water vapor from the Atlantic Ocean is mainly caused by anomalous winds during the months March-October. In contrast to LGM.O, the experiment LGM.N with the 3 K tropical cooling relative to CLIMAP shows only a slightly enhanced water vapor transport out of the tropical Atlantic area (Table 1). This mechanism is discussed later in section 4..

Interestingly, the interhemispheric water transport reduces drastically for both LGM.O and LGM.N, respectively. The strength of the meridional latent heat transport by the Hadley Cells is reduced by about 50% from the value obtained with the control integration (Figure 1a). This can be attributed in LGM.O and LGM.N to an anomalous southward component of latent heat transport by the southern hemispheric Hadley circulation over the Pacific and Indian Oceans (Plate 3).

3.3.3. Eddy moisture transport The strongest difference between the meridional transport of the LGM runs are in the extratropics of the Atlantic Ocean (Figure 1b). For LGM.O we observe a strong increased northward transport between 20° and 45°N for the LGM compared to the control integration. The increase in eddy moisture transport for LGM.O is strongest over the northwestern Atlantic centered at 30°N, 60°W (Plate 3). In LGM.N the eddy moisture transport shows only a slight increase (Figure 1b) between 20° and 45°N.

North of 50°N the temperature effect on moisture leads to a reduced eddy moisture transport for LGM.O and LGM.N. Corresponding with the drop in moisture transport (Figure 1b), we observe a band of midlatitude anomalous net precipitation (Figure 7a, and 7b) crossing the North Atlantic in northeast direction. This band is connected with the changed storm track position. The streamlines of water vapor transport in the northern North Atlantic are more southward and zonal during LGM.

Over the Southern Ocean the subtropical high provides enhanced export (Table 1). An anomalous low west of Madagascar (Plate 3) reduces the water vapor import to the Atlantic Ocean over South Africa (Table 1). This feature persists the entire year and is strongest during DJF.

4. Discussion

With our simulations of the different time slices, we calculate the atmospheric water transport and associated freshwater flux. In section 4.1. the present water cycle is discussed. Because the annual averaged hydrological cycle for the GI and CO experiments differs only slightly from the control integration, we concentrate on the Last Glacial Maximum climate simulations which are based on substantially differing SSTs as a lower boundary condition. The sensitivity experiments can be either used for comparison with proxy data available (section 4.2.) or for the analysis of mechanisms affecting the hydrological cycle (section 4.3.). It is also worthy to discuss the changes in the hydrological cycle in light of the implications for the oceanic circulation (section 4.4.).

4.1. Present Water Cycle

The model simulations provide a global picture for the atmospheric water cycle. For the present climate, the sources (subtropical highs) and sinks (e.g., high latitudes and the tropics) of water vapor and the streamflow component of water transport have been identified. A direct comparison of model simulation and data is difficult because the global freshwater flux is not well known in detail with large uncertainties arising from instrumental errors and sparse observational coverage [*Schmitt,* 1994; *Jourdan et al.,* 1997]. For the atmospheric water vapor transport the database is even worse.

When comparing zonal mean precipitation for the control integration, the climatological estimates of *Jaeger* [1976] and *Legates and Willmott* [1990], and ECMWF reanalysis data [*Gibson et al.,* 1997], the control simulation is within the range of climatological estimates (Figure 2). However, we detect some systematic errors in the ECHAM3 model in T42 resolution used here [*Roeckner et al.,* 1992]. The ITCZ over the oceans is simulated too far north (Figure 2). Over land, our model produces too much precipitation over Australia and South America compared with the climatological estimates [*Arpe et al.,* 1994]. Large uncertainties are over the Southern Ocean where the reanalysis provides a better estimate than the sparse estimates from observations. It should be further noted that the time periods of the observations, reanalysis, and AMIP data set are different which may cause differences, especially in the tropical Pacific Ocean.

The general structure of the vertically integrated meridional water vapor transport in Figure 1a is in agreement with observations [*Peixoto and Oort,* 1992]. The magnitude of the *Peixoto and Oort* [1992] transport is between ±0.6 Sv and therefore weaker than in our model. The modeled moisture transport over the

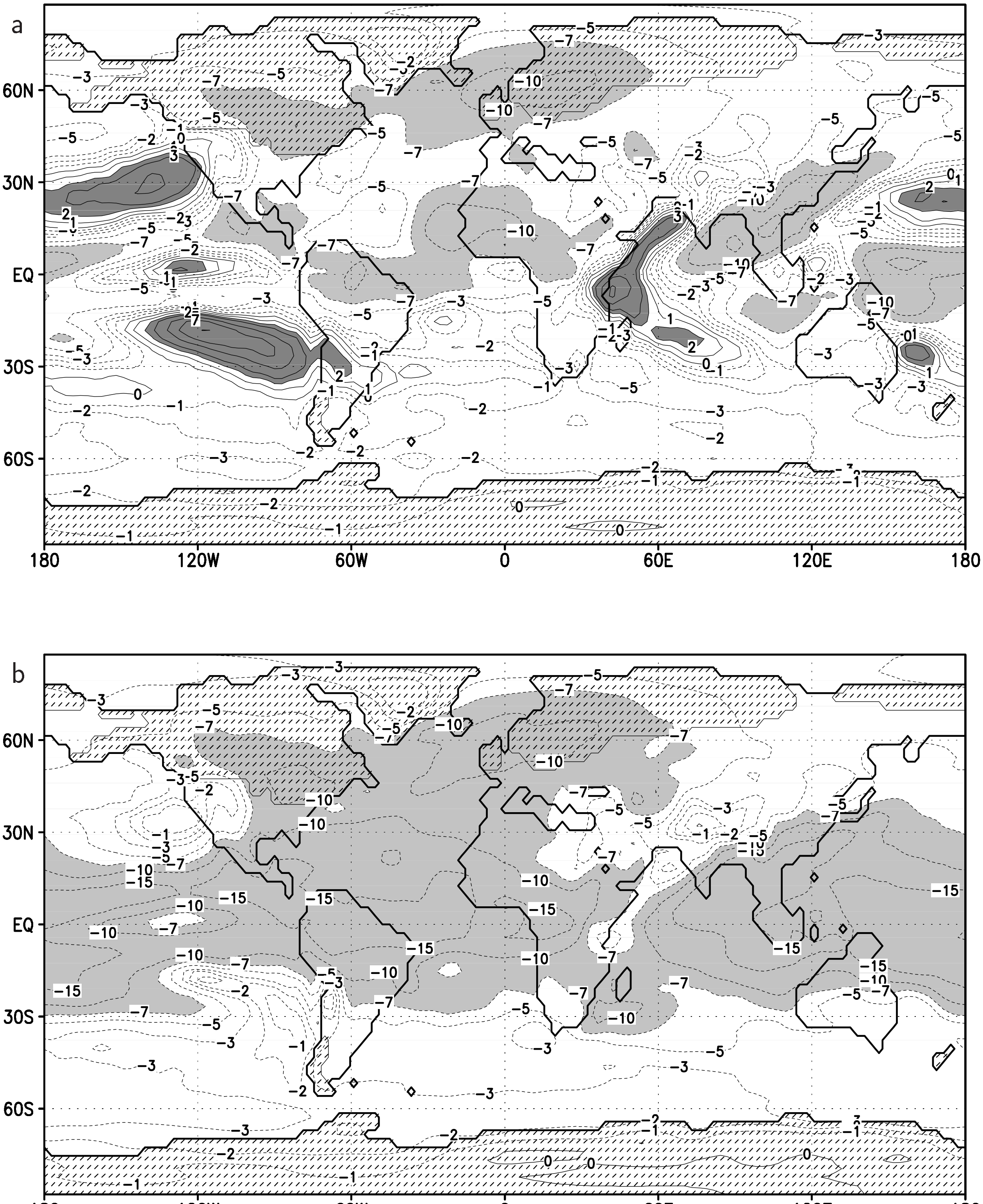

Figure 6: Anomalous glacial vertically integrated specific humidity for the runs (a) LGM.O and (b) LGM.N. The countour lines are at (±) 0, 1, 2, 3, 5, 7, 10, and 15 $\mathrm{kg\,m^{-2}}$ with humidity changes greater than +2 or less than −7 $\mathrm{kg\,m^{-2}}$ shaded darkly or lightly, respectively.

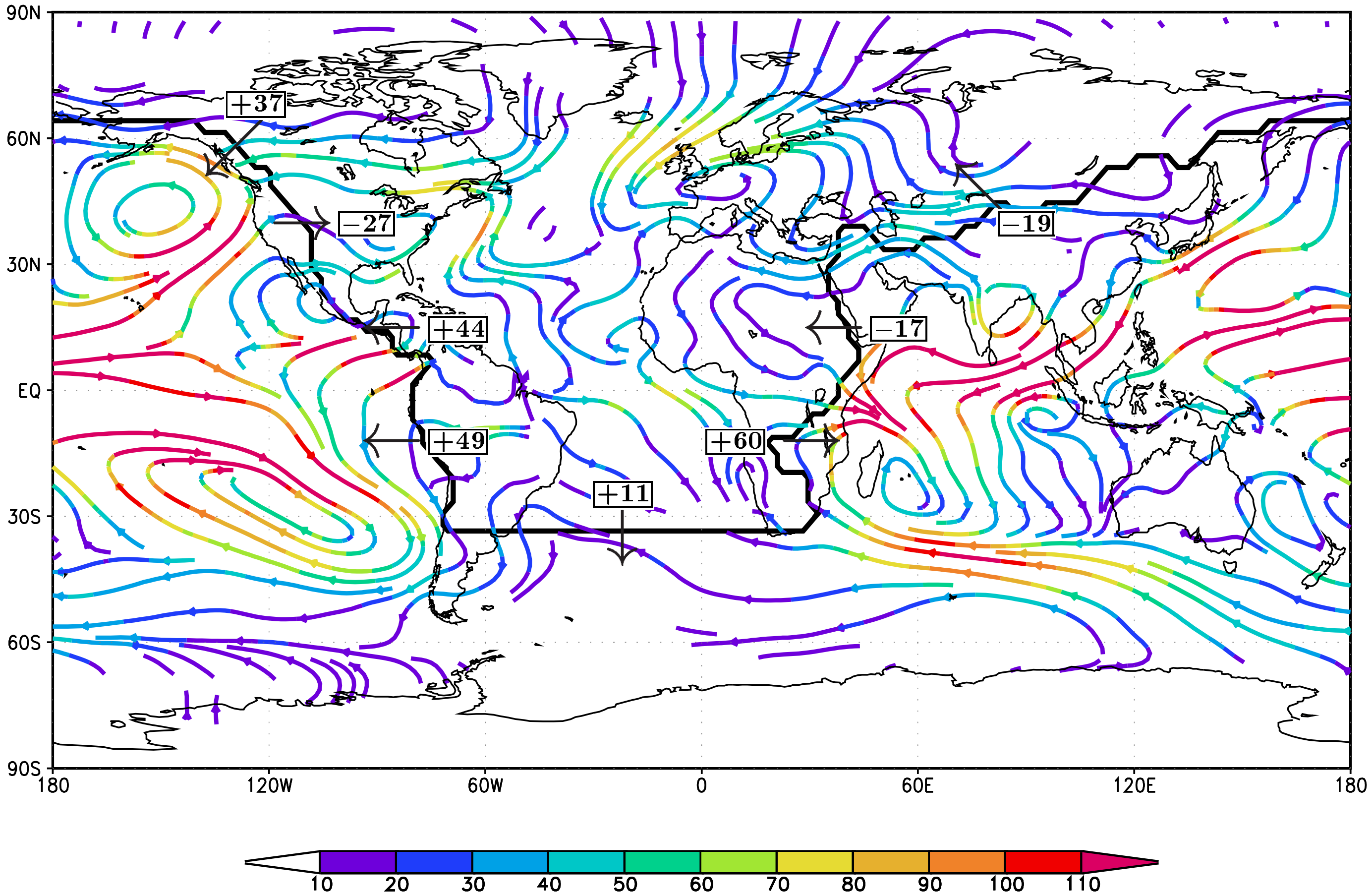

Plate 3. Anomalous horizontal freshwater transport in the atmosphere (LGM.O minus Control). Units are kg $m^{-1}s^{-1}$, where values below 10 kg $m^{-1}s^{-1}$ are suppressed. Arrows and numbers (10^6 kgs^{-1}=10^{-3} Sv) indicate the anomalous water mass transport out of the Atlantic catchment area over the respective drainage divides (compare Table 1).

drainage divides is similar with reanalysis data and previous modeling results [*Broecker et al.,* 1990; *Zaucker and Broecker,* 1992; *Wijffels et al.*, 1992]. The *Zaucker and Broecker* [1992] water vapor transport differs from ours in regional details which may be related to the spatial resolution and model physics. Another methodology has been applied by *Wijffels et al.* [1992] and *Jourdan et al.* [1997]. Using surface freshwater flux and runoff data, they confirm that the Indian and Atlantic Oceans are net evaporative basins, while the Pacific has a net gain of freshwater.

The asymmetry between the oceans for the interbasin transport of water vapor could be influenced by the distribution of landmasses on Earth. It is seen that low-latitude trade winds freely transport water vapor from the Atlantic to the Pacific over Central America, whereas the African continent have a drying influence on the water before the winds reach the continental divide. The low-latitude westward transport is more effective due to more moisture in the tropics than at high latitudes in the reverse direction. The import of water over North America is additionally blocked by the Rocky Mountains, whereas the eastward transport over Asia is relatively small due to the long way over the dry continent.

The different roles of Atlantic and Pacific Oceans for climate are intimately connected to the global hydrological cycle. In the ocean the characteristic residence time for salt exceeds millions of years which is far beyond the timescales considered here. Since there are no internal sources and sinks for salt in the ocean during the climate timescale of the late Quaternary, the net Atlantic export leads to relatively salty water in the Atlantic compared to the Pacific/Indian Oceans.

4.2. Comparison With Proxy Data for the LGM

A recent terrestrial data synthesis [*Farrera et al.,* 1999; *Kohfeld and Harrison,* 2000] contains quantitative reconstructions of mean temperature of the coldest month (MTCO) and mean annual ground temperature (MAT), and qualitative reconstructions of plant-available moisture (PAM) and runoff (P–E) from radiocarbon-dated terrestrial sites between 32°N and 33°S. This data set combines multiple indicators of quantitative changes in land surface temperature (pollen and plant macrofossil records of MTCO, and noble gas and speleothem records of MAT) and qualitative indicators of moisture balance parameters (pollen and plant macrofossil records of PAM and lake status records of P–E).

The temperature proxy data indicate a tropical and subtropical cooling by 4–6 K. The cooling was less in some sites in South and East Africa, India, and Indonesia [*Farrera et al.,* 1999]. The changes in MAT and MTCO at the LGM are broadly similar at low latitudes because the low seasonality of insolation in the tropics offers little scope for seasonal changes in temperature.

The reconstructed data are in good agreement with the temperature anomalies of LGM.N (Figure 4b). We notice that the LGM.N experiment captures a major part of the 5 K cooling (Figure 4b) inferred from the lowering of tropical snowlines on Hawaii, New Guinea, and Kilimanjaro (for a review, see *Crowley and North* [1991]). However, the validity of several features of tropical SSTs remain in question. Using new faunal SST reconstructions, *Hostetler and Mix* [1999] find a moderate warming over the subtropical gyres and a strong cooling over the eastern Atlantic and Pacific Oceans during LGM.

Reliable verification data for the hydrological cycle during glacial time are not available. Despite several uncertain factors affecting individual lakes, lake area, and depth vary monotonically with P–E. The reconstructed changes in lakes can therefore be used to infer the sign of changes in annual mean P–E (for a review, see *Farrera et al.* [1999]).

Plus and minus signs in Figure 7b indicate regions with strong changes in lake level as obtained from Global Lake Status Database [*Kohfeld and Harrison,* 2000]. According to the data, anomalous P–E is negative in the equatorial zone of America and the equatorial zone in western Africa, while anomalous P–E is positive in subtropical sites (Figure 7b). Other sites with moderate change in lake level (not shown) are in the eastern equatorial Africa, North America, and over Asia [*Farrera et al.*, 1999; *Kohfeld and Harrison*, 2000].

We find that the lake indicators shown in Figure 7b are in good agreement with P–E change of both LGM simulations (Figure 7). Furthermore, most sites with moderate change in lake level fit very well with the model results, whereas in two sites the proxy data change sign within one model grid cell. This shows that a direct comparison of point proxy data and model data can be extremely difficult in the presence of small-scale structure.

The equatorial ice-age aridity is probably responsible for an increase in windblown eolian sediments in equatorial Atlantic deep-sea sediment cores. Furthermore, concentration of feldspar originating from Amazon and Congo Rivers indicate dryer conditions over western Central Africa and equatorial South America. Since many regions on the continents are dryer during the LGM, a reduced acreage of swamps lowered atmospheric methane concentration.

The picture of the glacial hydrological cycle as obtained form the proxies (reviewed by *Crowley and North* [1991] and *Farrera et al.* [1999]) is consistent with experiment LGM.N (Figures 6b, 7b). A basic feature is the reduced equatorial precipitation (Figure 5) except for the western Indian Ocean and eastern Pacific regions (Figure 7) and ice-age aridity on the continents (Figure 6b).

Beside the terrestrial data, there are a few marine proxies for the hydrological cycle. Our analysis shows that during glacial times the atmospheric fresh water export out of the Atlantic was enhanced (Table 1) which is consistent with oxygen isotope records [*Broecker,* 1992] and increased salinity contrast between the Atlantic and the Pacific/Indian Oceans in ocean circulation experiments [*Winguth et al.,* 1999]. Furthermore, the anomalous positive P–E over the North Atlantic (Figure 7) is consistent with the δ^{18}O signal in planktonic foraminifera [*Dupplessy et al.,* 1991].

4.3. Mechanisms Affecting the Hydrological Cycle

In section 3.3. we identified three mechanisms affecting the hydrological cycle in LGM simulations to be discussed here. The continental drying effect over North America is related to the altered ice-sheets during LGM. For the control run, LGM.O, and LGM.N, the transport over the continental landmasses (Asia, Africa, America) is weaker (Table 1), the dryer the continental areas.

The changed hydrological cycle in the tropics is caused by circulation changes associated with SST anomalies and corresponding anomalous rainfall. *Wu and Liu* [1992] have examined the anomalous moisture convergence in an AGCM with respect to SST anomalies in the Pacific Ocean. Over a warm SST anomaly region, the circulation is more cyclonic in the lower troposphere and more anticyclonic in the upper troposphere. The near-surface moisture convergence is largely associated with SST and specific humidity anomaly fields: $\vec{v}\, q \sim q\ \nabla$SST. Intensified ascent occurs over the warm SST anomaly region and the anomalous rainfall is typically 3 to 4 times as large as the anomalous evaporation.

Since the specific humidity is concentrated near the surface, the lower tropospheric moisture transport is well represented by the vertically integrated water vapor transport. We see that the streamlines of Plate 3 coincide with the contours of specific humidity (Figure 6a) and SST (Plate 1b). For LGM.O we find that the anomalous water vapor divergence (Figure 3) is directed towards warm SST anomaly (Plate 1b) causing anomalous freshwater flux (Figure 7a).

Thus, the enhanced Atlantic water vapor export can be explored by the relatively warm Pacific and Indian

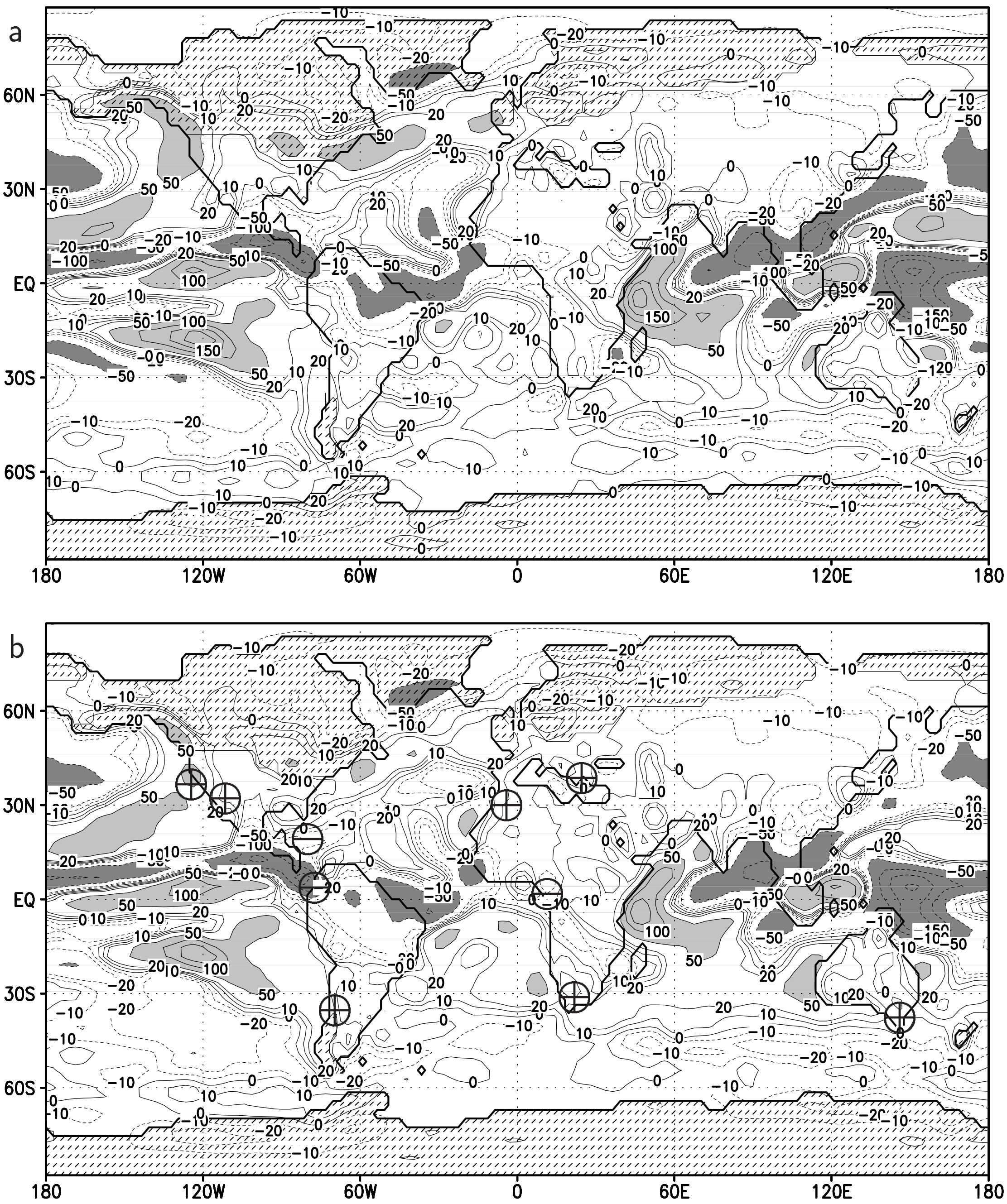

Figure 7: Anomalous glacial precipitation minus evaporation (mm/month) for the runs (a) LGM.O and (b) LGM.N. The contour lines are as in Figure 3. (b) Plus and minus signs indicate reconstructed changes in annual mean P–E as supplied by lake levels [after *Kohfeld and Harrison*, 2000, Figure 1b].

Oceans compared with the anomalous cold Atlantic Oceans. In LGM.N, however, the reduced tropical humidity relative to LGM.O causes a drop in westerly water vapor transport over Africa and Central America (Table 1) consistent with the theory.

The differences in the Atlantic extratropical transport (Figure 1b) are based on changes in baroclinicity in the lower layers of the atmosphere (for a detailed discussion, see *Hall et al.* [1996] and *Dong and Valdes* [1998]). The associated eddy moisture transport in midlatitudes, related to the meridional moisture gradient (Figure 6), is strongly enhanced for LGM.O and is only slightly changed for LGM.N relative to the control run (Figure 1b). The associated net precipitation rates are higher for LGM.O than in LGM.N (Figure 7). It is furthermore found that glacial precipitation rates at northern polar latitudes are almost zero during DJF and are reduced by 50% relative to the control run during JJA. This asymmetry in the seasonal cycle is essential for the interpretation of Greenland's ice core water isotopic compositions [*Werner et al.,* 2000].

4.4. Implications for the Ocean Circulation

Since mass is conserved within the climate system, the atmospheric mass transport (Figure 1a) implies an oceanic mass transport when assuming a negligible northward mass transport by the rivers and glaciers. This assumption is not very strong, because the characteristic time scale for the barotropic oceanic mass transport is very fast due to waves. Furthermore, we can assume a quasi-equilibrium for the mass stored in the ice sheets for our time slices considered. The atmospheric water transport in the Atlantic catchment area (Figure 1b) should be exactly balanced with the oceanic transport when subtracting the Bering Strait throughflow. Since the Bering Strait throughflow into the Atlantic Ocean is about 0.8 Sv for the present climate [*Wijffels et al.,* 1992], the Atlantic Ocean vertically integrated ocean mass transport is southward at all latitudes. For the LGM the Bering Strait is closed, and the implied oceanic mass transport changes the direction (Figure 1b).

The implied oceanic heat and mass transport in the Atlantic provide a constraint for the vertically integrated oceanic circulation [*Lohmann et al.,* 1996]. Integrating the surface oceanic heat flux starting from the North Pole, the implied oceanic heat transport in the Atlantic Ocean can be obtained [*Webb et al.,* 1997]. The analysis yields an oceanic heat transport in the Atlantic Ocean at 20°N of 1.0, 0.7, and 0.6 PW for the Control, LGM.N, and LGM.O experiments, respectively. The difference between the two LGM runs originates from an increased oceanic heat loss over the North Atlantic Ocean in LGM.N compared to LGM.O. The reduction of meridional heat transport during LGM is consistent with oceanic simulations of the LGM [*Winguth et al.,* 1999].

Another important implication for the ocean considers the sensitivity of the Atlantic's conveyor belt circulation. Numerical experiments suggest that the strength of the THC in the Atlantic depends on the net amount of freshwater leaving the Atlantic catchment [*Zaucker et al.,* 1994; *Rahmstorf,* 1996]. The enhanced Atlantic water vapor export during glacial times would therefore give a stabilizing effect for the THC. This effect is strong for LGM.O (0.138 Sv) and relatively weak for LGM.N (0.033 Sv). In our experiments we identified the tropical interoceanic transport (Atlantic-Pacific) as an important mechanism affecting the freshwater forcing. The tropical Atlantic (30°S – 30°N) has an anomalous freshwater export of 0.274 Sv for LGM.O and 0.035 Sv for LGM.N (Table 1).

We find that the Atlantic receives more freshwater north of 30°N in the LGM.O experiment than in the control integration (0.136 Sv), whereas the net northern Atlantic freshening in LGM.N is negligible (0.002 Sv). Furthermore, sea ice transport from the Arctic Ocean contributes to a freshwater input into the North Atlantic (about 0.1 Sv for the present climate) and provides a link between Arctic and North Atlantic [*Hilmer et al.,* 1998].

For comparison, the peak deglacial meltwater discharge, which probably interrupted the North Atlantic Deep Water formation, reached 0.44 Sv [*Fairbanks,* 1989]. Coupled atmosphere-ocean model scenarios suggest that the net precipitation in the northern North Atlantic is expected to increase by about 0.1 Sv for a quadrupling of CO_2 [*Manabe and Stouffer,* 1994]. *Rahmstorf* [1996] gives a critical freshwater threshold of 0.07 Sv for slowing down the present-day circulation. A similar threshold evaluates *Weaver et al.* [1998] by increasing the Rhine catchment at the expense of the Amur and Yangtze-Yellow Rivers. To relate these numbers to the present land ice volume, a rate of 0.08 Sv over 10 kyr corresponds to total melting of the ice sheets.

5. Conclusions

The simulation of paleoclimates provides an excellent test for atmospheric circulation models under different boundary conditions. Because the atmospheric branch of the hydrological cycle is responsible for important feedbacks in the climate system, it is important to analyze the water vapor transport and associated freshwater flux for different climatic conditions. The experiments with present-day SSTs and changed insolation (GI and CO) show mainly an altered seasonality (e.g., monsoon circulation) compared with the control run. The annual averaged water transport in these experiments is found to be close to the Control run. Because the hydrological cycle during the Last Glacial Maximum shows strong deviations from the present hydrological cycle, we have concentrated on this time slice.

One simulation of the Last Glacial Maximum is forced with the CLIMAP reconstruction (LGM.O), whereas our new simulation (LGM.N) is forced by colder tropical temperatures relative to CLIMAP. This tropical cooling is motivated by recent data and modeling studies [*Guilderson et al.,* 1994; *Stute et al.,* 1995; *Schrag et al.,* 1996; *Bard et al.,* 1997; *Ganopolski et al.,* 1998; *Farrera et al.,* 1999]. Because the agreement in LGM.N with the proxy data is much better than LGM.O, we conclude the lowered tropical temperatures provide a more consistent picture of the glacial terrestrial climate.

Because of the temperature effect on moisture, the largest part of the Atlantic water vapor transport is in the tropics. We find that this transport is strongly related to the large-scale temperature pattern, where anomalous precipitation during LGM is biased towards the relatively warm Indian and Pacific Oceans. Our analysis suggests that changes in the equatorial ocean, which may be related to variability of the eastern equatorial Pacific as a climatic sensitive region [*Pisias and Mix,* 1997], are extremely important for estimating the water vapor routes and their variability during glacial times.

Our simulations indicate the strong influence of tropical SSTs on glacial climate. Recent data from marine sediments suggest warmer SSTs and less sea ice in the northern North Atlantic relative to CLIMAP which would imply an oceanic circulation with deep water formation in the Nordic Seas during LGM [*Weinelt et al.,* 1996]. These studies emphasize the importance of updated SST reconstructions and indicate that the glacial climate cannot be sufficiently understood without explicitly considering the feedbacks associated with the ocean, ice, vegetation and other components of the land-surface.

Interactive changes in vegetation types have been neglected in our study. Vegetation affects heat and moisture balances feeding back to other climate components [*Foley et al.,* 1998]. Recently, experiments simulating LGM climate including biome representation [*Crowley and Baum,* 1997; *Kubatzki and Claussen,* 1998] emphasize the influence of a biosphere-atmosphere interaction on the simulated climate.

The atmospheric water transport with its high mobility is one of the most sensitive parts in the coupling of three-dimensional atmosphere and ocean models. Although the hydrological cycle with its characteristically small spatial scales is notoriously difficult to obtain, it determines to a large extent the flow regime of the large-scale thermohaline circulation [*Rahmstorf,* 1995; *Weaver et al.,* 1998] and may trigger rapid transitions of past and future climate change. A negative mass balance in the Atlantic could contribute to reorganizing the atmosphere-ocean system and stabilizing THC (G. Lohmann, et al., On the global water cycle and the thermohaline circulation: Analysis of a coupled general circulation model, submitted to *Atmosphere-Ocean,* 2000). Our experiments and analysis for different time slices of the late Quaternary provide a necessary first step to understand the water cycle and related feedbacks, which will be the subject of further investigations.

Acknowledgments C. Heinze, K. Rodgers, K. Herterich, M. Werner, and M. Heimann are gratefully acknowledged for helpful suggestions improving the manuscript. Thanks go furthermore to U. Wyputta, S. Harrison, and K. Arpe providing us with part of the data. This work was partly supported by BMBF through WOCE, CLIVAR, and Klimaforschungsprogramm.

References

Arpe, K., L. Bengtsson, L. Dümenil, and E. Roeckner, The hydrological cycle in the ECHAM3 simulations of the atmospheric circulation, in *Global Precipitation and Climate Change, NATO ASI Ser.,* vol. *26*, edited by M. Desbois and F. Désalmand, pp. 361–377, Springer-Verlag, New York, 1994.

Bard, E., F. Rostek, and C. Sonzogni, Interhemispheric synchrony of the last deglaciation inferred from alkenone paleothermometry, *Nature, 385,* 707–710, 1997.

Barnola, J. M., D. Raymond, Y. S. Korotkevich, and C. Lorius, Vostok ice core provides 160,000-year record of atmospheric CO_2, *Nature, 329,* 408–414, 1987.

Baumgartner, A., and E. Reichel, *The World Water Balance,* Elsevier, New York, 1975.

Berger, A. L., Long-term variations of daily insolation and Quaternary climatic changes, *J. Atmos. Sci., 35,* 2362–2367, 1978.

Birchfield, E. G., A coupled ocean-atmosphere climate model: temperature versus salinity effects on the thermohaline circulation, *Clim. Dyn., 4,* 57–71, 1989.

Broccoli, A. J., and E. P. Marciniak, Comparing simulated glacial climate and paleodata: A reexamination, *Paleoceanography, 11,* 3–14, 1996.

Broecker, W. S., The salinity contrast between the Atlantic and Pacific during glacial time, *Paleoceanography, 4*, 207–212, 1992.

Broecker, W. S., T. H. Peng, J. Jouzel, and G. Russel, The magnitude of global freshwater transports of importance to ocean circulation, *Clim. Dyn., 4*, 73–79, 1990.

CLIMAP Project Members, The surface of the ice age Earth, *Science, 191,* 1131–1137, 1976.

CLIMAP Project Members, Seasonal reconstructions of the Earth surface at the last glacial maximum, *Geol. Soc. Am. Map Chart Ser., MC-36,* Boulder, Colo., 1981.

Crowley, T. J., and S. K. Baum, Effect of vegetation on an ice-age climate model simulation, *J. Geophys. Res., 102,* 16,463–16,480, 1997.

Crowley, T. J., and G. R. North, *Paleoclimatology,* 339 pp., New York, 1991.

Dansgaard, W., et al., Evidence for general instability of past climate from a 250-kyr ice-core record, *Nature, 364*, 218–220, 1993.

Dong, B., and P. J. Valdes, Simulations of the Last Glacial Maximum climates using a general circulation model: Prescribed versus computed sea surface temperatures, *Clim. Dyn., 14*, 571–591, 1998.

Dupplessy, J.-C., L. D. Labeyrie, A. Juillet-Leclerc, F. Maitre, J. Dupart, and M. Sarnthein, Surface salinity reconstruction of the North Atlantic Ocean during the Last Glacial Maximum, *Oceanol. Acta, 14,* 311–324, 1991.

Fairbanks, R. G., A 17,000-year glacio-eustatic sea level record: Influence of glacial melting rates on the Younger Dryas event and deep-ocean circulation, *Nature, 342,* 637–642, 1989.

Farrera, I., et al., Tropical palaeoclimates at the Last Glacial Maximum: A new synthesis of terrestrial data, *Clim. Dyn., 15,* 823–856, 1999.

Foley, J. A., S. Levis, I. C. Prentice, D. Pollard and S. L. Thompson, Coupling dynamic models of climate and vegetation. *Global Change Biol., 4,* 561–579, 1998.

Ganopolski, A., S. Rahmstorf, V. Petouhov, and M. Claussen, Simulation of modern and glacial climates with a coupled global model of intermediate complexity, *Nature, 391,* 351–356, 1998.

Gates, W. L., The Atmospheric Model Intercomparison Project, *Bull. Am. Meteorol. Soc., 73,* 1962–1970, 1992.

Gibson, J. K., P. Kållberg, S. Uppala, A. Hernandez, A. Nomura, and E. Serrano, *ECMWF Reanalysis Project Report Series,* vol. *1, ERA Description,* 71 pp., Eur. Cent. for Medium-Range Weather Forecasts, Reading, England, 1997.

Graham, N. E., and T. P. Barnett, Sea surface temperature, surface wind divergence, and convection over tropical oceans, *Science, 238,* 657–659, 1987.

Guilderson, T. P., R. G. Fairbanks, and J. C. Rubenstone, Tropical temperature variations since 20,000 years ago: Modulating interhemispheric climate change, *Science, 263,* 663–665, 1994.

Hall, M. J., B. Dong, and P. J. Valdes, Atmospheric equilibrium, instability and energy transport at the last glacial maximum, *Clim. Dyn., 12,* 497–511, 1996.

Hays, J. D., J. Imbrie, and N. J. Shackelton, Variations in the Earth's Orbit: Pacemaker of the Ice Ages, *Science, 194,* 1121–1132, 1976.

Hilmer, M., M. Harder, and P. Lemke, Sea ice transport: A highly variable link between Arctic and North Atlantic, *Geophys. Res. Lett., 25,* 3359–3362, 1998.

Hostetler, S. W., and A. C. Mix, Reassessment of ice-age cooling of the tropical ocean and atmosphere, *Nature, 399,* 673–676, 1999.

Imbrie, J. J., D. Hays, D. G. Martinson, A. McIntyre, A. C. Mix, J. J. Morley, N. G. Pisias, W. L. Prell, and N. J. Shackleton, The orbital theory of Pleistocene climate: Support from a revised chronology of the marine δ^{18}O record, in *Milanković and Climate,* edited by A. Berger, J. Imbrie, J. Hays, G. Kukla, and B. Saltzman, pp. 269–305, D. Reidel, Norwell, Mass., 1984.

Jaeger, L., Monatskarten des Niederschlags für die ganze Erde. *Ger. Weather Serv. Rep. 139,* Offenbach, 1976.

Jourdan, D., P. Peterson, and C. Gautier, Oceanic freshwater budget and transport as derived from satellite radiometric data, *J. Phys. Oceanogr., 27,* 457–467, 1997.

Joussaume, S., and K. E. Taylor, Status of the Paleoclimate Modeling Intercomparison Project (PMIP), in *Proceedings of the First International AMIP Scientific Conference*, pp. 425–430, World Clim. Res. Program, vol. *92,* Geneva, 1995.

Kohfeld, K., and S. P. Harrison, How well can we simulate past climates? Evaluating the models using global palaeoenvironmental data sets, *Quat. Sci. Rev., 19,* 321–346, 2000.

Kubatzki, C., and M. Claussen, Simulation of the global bio-geophysical interactions during the Last Glacial Maximum, *Clim. Dyn., 14,* 461–471, 1998.

Legates, D. R., and C. D. Willmott, Mean seasonal and spatial variability in gauge-corrected global precipitation. *Int. J. Climatol., 9,* 111-127, 1990.

Lehman, S. J., and L. D. Keigwin, Sudden changes in North Atlantic circulation during the last deglaciation, *Nature, 356,* 757–762, 1992.

Lohmann, G., R. Gerdes, and D. Chen, Sensitivity of the thermohaline circulation in coupled oceanic GCM – atmospheric EBM experiments, *Clim. Dyn., 12,* 403–416, 1996.

Lorenz, S., B. Grieger, P. Helbig, and K. Herterich, Investigating the sensitivity of the Atmospheric General Circulation Model ECHAM3 to paleoclimatic boundary conditions, *Geol. Rundsch., 85,* 513–524, 1996.

Manabe, S., and R. J. Stouffer, Multiple-century response of a coupled ocean-atmosphere model to an increase of the atmospheric carbon dioxide, *J. Climate, 7,* 5–23, 1994.

Manabe, S., and R. J. Stouffer, Simulating of abrupt climate change induced by freshwater input into the North Atlantic Ocean, *Nature, 378,* 165–167, 1995.

Mayewski, P. A., L. D. Meeker, S. Whitlow, M. S. Twickler, M. C. Morrison, R. B. Alley, P. Bloomfield, and K. Taylor, The atmosphere during the Younger Dryas, *Science, 261,* 195–197, 1993.

Milanković, M., Kanon der Erdbestrahlung, *Spec. Publ. 132,* vol. *33,* Sect. Math. Nat. Sci., R. Serb. Acad., Belgrade, 1941.

Peixoto, J. P., and A. H. Oort, *Physics of Climate,* 520 pp., Am. Inst. of Phys., 1992.

Peltier, W. R., Ice age paleotopography, *Science, 265,* 185–201, 1994.

Pisias, N. G, and A. C. Mix, Spatial and temporal oceanographic variability of the eastern equatorial Pacific during the late Pleistocene: Evidence from Radiolaria microfossils, *Paleoceanography, 12,* 381–393, 1997.

Prange, M., G. Lohmann, and R. Gerdes, Sensitivity of the thermohaline circulation for different climates – Investigations with a simple atmosphere-ocean model. *Palaeoclimates, 2*, 79–99, 1997.

Rahmstorf, S., Bifurcations of the Atlantic thermohaline circulation in response to changes in the hydrological cycle, *Nature, 378*, 145–149, 1995.

Rahmstorf, S., On the freshwater forcing and transport of the Atlantic thermohaline circulation, *Clim. Dyn., 12*, 799–811, 1996.

Roeckner, E., et al., Simulation of the present-day climate with the ECHAM model: Impact of model physics and resolution, *MPI Rep. 93,* Hamburg, Germany, 1992.

Schmitt, R. W., The ocean freshwater cycle, in *CCCO-JSC Ocean Observing System Development Panel*, 32 pp., Texas A&M Univ., College Station, 1994.

Schrag, D. P., G. Hampt, and D. W. Murray, Pore fluid constraints on the temperature and oxygen isotopic composition of the glacial ocean, *Science, 272,* 1930–1932, 1996.

Stute, M., M. Forster, H. Frischkorn, A. Serejo, J. F. Clark, P. Schlosser, W. S. Broecker, and G. Bonani, Cooling of tropical Brazil (5°C) during the Last Glacial Maximum, *Science, 269,* 379–383, 1995.

Warren, B. A., Why is no deep water formed in the North Pacific?, *J. Mar. Res., 41*, 327–347, 1983.

Weaver, A. J., M. Eby, A. F. Fanning, and E. C. Wiebe, Simulated influence of carbon dioxide, orbital forcing and ice sheets on the climate of the Last Glacial Maximum, *Nature, 394,* 847–853, 1998.

Webb, R. S., S. J. Lehman, R. J. Healy, and D. Sigman, Influence of ocean heat transport on the climate of *Nature, 385,* 695–699, 1997.

Weinelt, M., M. Sarnthein, U. Pflaumann, H. Schulz, S. Jung, and H. Erlenkeuser, Ice-free nordic seas during the last glacial maximum? Potential sites of deepwater formation, *Palaeoclimates, 1,* 283–309, 1996.

Werner, M., U. Mikolajewicz, M. Heimann, and G. Hoffmann, Borehole versus isotope temperatures on Greenland: seasonality does matter, *Geophys. Res. Lett., 27*, 723–726, 2000.

Wijffels, S. E., R. W. Schmitt, H. L. Bryden, and A. Stigebrandt, Transport of fresh water by the oceans, *J. Phys. Oceanogr., 22*, 155–162, 1992.

Winguth, A., D. Archer, E. Maier-Reimer, U. Mikolajewicz, and J.-C. Dupplessy, Sensitivity of the paleonutrient tracer distribution and deep-sea circulation to glacial boundary conditions, *Paleoceanography, 14*, 304–323, 1999.

Wu, G., and H. Liu, Atmospheric precipitation in response to equatorial and tropical sea surface temperature anomalies, *J. Atmos. Sci., 49*, 2236–2255, 1992.

Zaucker, F., and W. S. Broecker, The influence of atmospheric moisture transport on fresh water balance of the Atlantic drainage basin: General circulation model simulations and observations, *J. Geophys. Res., 97*, 2765–2773, 1992.

Zaucker, F., T. F. Stocker, and W. S. Broecker, Atmospheric freshwater fluxes and their effect on the global thermohaline circulation, *J. Geophys. Res., 99*, 12,443–12,457, 1994.

G. Lohmann, Max-Planck-Institut für Meteorologie, Bundesstrasse 55, 20146 Hamburg, Germany. (e-mail: gerrit.lohmann@dkrz.de)

S. Lorenz, Department of Geoscience, University of Bremen, Klagenfurter Straße, 28359 Bremen, Germany. (e-mail: slor@palmod.uni-bremen.de)

Received August 5, 1999; revised February 11, 2000; accepted February 16, 2000.